Computational and Structural Biotechnology Journal 21 (2023) 601–613

Contents lists available at ScienceDirect

Computational and Structural Biotechnology Journal

journal homepage: www.elsevier.com/locate/csbj

Design of nanobody-based bispecific constructs by *in silico* affinity maturation and umbrella sampling simulations

Zixuan Bai [a,b,1], Jiewen Wang [a,b,c,1], Jiaqi Li [a,b,c], Haibin Yuan [a,b], Ping Wang [d], Miao Zhang [a,b,e], Yuanhang Feng [a,b], Xiangtong Cao [b], Xiangan Cao [b], Guangbo Kang [a,b,c,*], Ario de Marco [f,**], He Huang [a,b,c,*]

[a] Department of Biochemical Engineering, School of Chemical Engineering and Technology, Tianjin University, Tianjin 300350, China
[b] Frontiers Science Center for Synthetic Biology and Key Laboratory of Systems Bioengineering (Ministry of Education), Tianjin University, Tianjin 300072, China
[c] Institute of Shaoxing, Tianjin University, Zhejiang 312300, China
[d] Tianjin Modern Innovative TCM Technology Co. Ltd., Tianjin, China
[e] China Resources Biopharmaceutical Company Limited, Beijing, China
[f] Laboratory for Environmental and Life Sciences, University of Nova Gorica, Nova Gorica, Slovenia

ARTICLE INFO

Article history:
Received 13 June 2022
Received in revised form 14 December 2022
Accepted 14 December 2022
Available online 16 December 2022

Keywords:
Bispecific construct
Rational affinity maturation
Umbrella sampling simulation
TNF-α
IL-23

ABSTRACT

Random mutagenesis is the natural opportunity for proteins to evolve and biotechnologically it has been exploited to create diversity and identify variants with improved characteristics in the mutant pools. Rational mutagenesis based on biophysical assumptions and supported by computational power has been proposed as a faster and more predictable strategy to reach the same aim. In this work we confirm that substantial improvements in terms of both affinity and stability of nanobodies can be obtained by using combinations of algorithms, even for binders with already high affinity and elevated thermal stability. Furthermore, *in silico* approaches allowed the development of an optimized bispecific construct able to bind simultaneously the two clinically relevant antigens TNF-α and IL-23 and, by means of its enhanced avidity, to inhibit effectively the apoptosis of TNF-α-sensitive L929 cells. The results revealed that salt bridges, hydrogen bonds, aromatic-aromatic and cation-pi interactions had a critical role in increasing affinity. We provided a platform for the construction of high-affinity bispecific constructs based on nanobodies that can have relevant applications for the control of all those biological mechanisms in which more than a single antigen must be targeted to increase the treatment effectiveness and avoid resistance mechanisms.

1. Introduction

The term inflammatory bowel disease (IBD) refers to a group of pathological conditions characterized by chronic, remittent and relapsing gastrointestinal inflammation, which leads to intestinal fibrosis and a variety of complications, including strictures, abscesses, fistulas, but also extraintestinal manifestations and colitis-related tumors. Based on the site and phenotype, IBD is classified as Crohn's disease or ulcerative colitis [1,2] and represents a major medical burden worldwide, with the highest incidence in Europe and North America but rising incidence in Asia [3]. IBD treatment with conventional anti-inflammatory drugs has posed problems of intolerance [4] and, therefore, there is an evident interest for alternative curative approaches, such as anti-TNFα, anti-α4β7 or anti-IL23 antibodies that have the capacity to inhibit proteins involved into the disease progression [5–9]. Tumor necrosis factor (TNF) is a pro-inflammatory cytokine that acts as a mediator of the autoimmune process and anti-TNF therapy has showed promising results, despite up to 40 % of the patients did not respond to the drug when used alone [10–12]. IL-23 favors the proliferation of T helper 17 cells in tissue inflammation and could therefore represent a further pro-inflammatory mediator. Interestingly, it was observed that anti-TNF resistance could be successfully overcome by anti-IL-23 treatments

* Corresponding authors at: Department of Biochemical Engineering, School of Chemical Engineering and Technology, Tianjin University, Tianjin 300350, China.
** Corresponding author.
E-mail addresses: 218111@tju.edu.cn (G. Kang), ario.demarco@ung.si (A. de Marco), huang@tju.edu.cn (H. Huang).
[1] These authors contributed equally to this work.

https://doi.org/10.1016/j.csbj.2022.12.021

with risankizumab and MEDI2070 antibodies [13–15]. Clinical trials have shown that dual-target therapy exploiting ustekinumab (anti-IL-23) and adalimumab (anti-TNF-α) improved both intestinal and extraintestinal symptoms in most IBD patients without significant safety issues [16]. In this perspective, the development of bispecific antibodies targeting simultaneously both antigens might be considered a logic development, similarly to what already positively tested in the case of other diseases [17]. Since such dual-activity molecules are technically difficult to prepare with IgG, recombinant antibody fragments represent a convenient alternative to produce multi-specific binders the realization of which requires extensive engineering [18]. The availability of a bifunctional molecule, instead of two independent binders, might also simplify the drug characterization since it will halve the work and avoid dealing with unpredictable interferences between the two single molecules. We prefer talking of bifunctional molecules rather than bispecific to underline that, in the absence of structural studies demonstrating the actual capacity to bind simultaneously to both targets, the peculiarity of such construct is suitability to interfere with two independent signaling pathways rather than binding to distinct antigens at the same time.

Nanobodies are particularly suited for this application because of their bio-physical properties and their short sequence that requires less computational power for identifying the key residues necessary for their maturation into optimized reagents [19–22]. Affinity is a critical factor for therapeutic drugs and antibody binding affinity used in clinical applications usually have K_D values below 1 nM [23]. Nanobodies can reach binding affinities in the low pM range but several binders that are potentially interesting because of their selectivity or epitope preference might have insufficient affinity for their antigens. The conventional approach for their in vitro maturation foresees a preliminary step of random mutagenesis followed by rounds of panning performed under stringent conditions using the mutant library. Computer-assisted *in silico* affinity maturation represents a valuable alternative under rapid development that uses protein structure-based rational design and algorithm optimization to reach its goals [24,25]. By applying the ADAPT platform, we recovered a nanobody mutant (Nb02-M7) the binding affinity of which for its antigen CD47 was enhanced 87.4-folds [26,27], whereas the VIMAS platform allowed obtaining an anti-HIF-1 mutant (VHH212-M3) with 17.5-fold higher affinity with respect to the original nanobody [28,29].

Nanobodies VHH2 against TNF-α and 37D5 against IL23 were originally obtained panning libraries prepared starting from immunized llamas [30,31]. In this work we first describe an approach to rationally mutate them and increase their affinity. Then we combined pairs of nanobodies into bifunctional molecules active on both antigens. This conceptually new approach overcomes previous contributions in which multivalent nanobody-based molecules were developed exclusively against either TNF-α or IL-23 [30,31].

2. Results

2.1. Analysis of the residues involved in the antigen-nanobody interfaces

Our approach limits the mutagenesis to the residues involved in the antigen recognition to reduce the impact on the molecule stability and maintain the mutant number small enough to be able to characterize them experimentally. Therefore, the first effort of our work was the identification of the amino acids composing the interface between the single nanobodies and their specific antigens. The application of the InterProSurf program to the available structural data of the nanobodies VHH2 and 37D5 as well as of their corresponding antigens TNF-α and IL-23 allowed localizing the key residues involved in the antigen-antibody interactions (Table 1). The amino acids of nanobody and antigen involved in docking are displayed as sticks in Fig. 1A-B.

Table 1
Amino acids involved in the interface of the complexes VHH2/TNF-α and 37D5/IL-23 according to the predictions of the InterProSurf program.

Proteins	Key residues
VHH2	N31, Y32, W33, Y35, E50, T53, N54, L56, I57, K59, R98, S99, F103
37D5	T28, Y31, L32, S52, Y57, E101, Y103, R106, Y108, E112
TNF-α	L75, T77, T79, Y87, Q88, T89, K90, V91, N92, I97, E135, I136, N137
IL-23	K20, T23, L24, W26, S27, A28, H29, P30, L31, P94, S95, L96, L97, P98, D99, P101, Q104, L140, F144

2.2. In silico optimization of nanobody biophysical characteristics

VIMAS was utilized to estimate the mutant binding free energy (a parameter related to affinity) and total energy (a factor indicative of stability). For VHH2, each of the 13 residues identified by InterProSurf was let exchange with any other amino acid (excluding cysteine and proline, namely 17 options). The resulting 221 single-residue mutations were examined by the three independent methods mCSM-AB, OSPREY and FoldX [32–34], with the results presented in Supplementary Tables S1, S2, S3, and S4, respectively. The results obtained applying each of the software were then combined and enabled to identify eight consensus single-mutations that involved three residues (N31, E50, and T53, Fig. 1 C). In the case of 37D5, the same protocol allowed spotting three single-mutations in three residues (T28, Y31, Y108, Fig. 1D and Supplementary Table S5, S6, S7, and S8).

The effect of amino acid mutations on the nanobody solubility was further evaluated by means of the Camsol online server (Table 2) that attributed solubility scores to both wild type and mutant clones. According to this prediction, most of the mutations have lower solubility than the wild type nanobodies. In particular, the transformation of the polar amino acid N31 of VHH2 into Trp and Phe, two non-polar amino acids, was predicted to reduce dramatically the intrinsic solubility of the mutants, from 0.382 to − 0.078 and − 0.068, respectively. Consequently, these two mutants were eliminated.

Next, in round 2, single mutations were combined to identify candidates with two mutated residues. For VHH2, eight double residue mutants were formed by combining six single point mutations, and three double residue mutants were also obtained for 37D5 (Fig. 1C-D). Their binding free energy was estimated by FoldX and the negative ΔΔG variations predicted that mutants had increased affinity (Fig. 1C-D). In parallel, the solubility of the double residue mutants was evaluated by the Camsol (Supplementary Table S9). Altogether, the *in silico* assessment enabled to select eight double-residue mutants for VHH2 and a double mutant and three single mutants for 37D5 that were validated experimentally. When the procedure was applied to combine three single mutations, no improved variant was identified, as assessed by FoldX (data not shown).

Recombinant expression of both wildtype and mutant nanobodies was performed in bacteria and a two-step purification protocol (metal affinity + gel filtration) provided almost homogeneous proteins of the expected mass (Supplementary Fig. S1) with yields in the range of 0.48–7.5 mg/l (Supplementary Fig. S1 and Table S10). In this step, four double point mutants of VHH2 were eliminated due to low yield. The *in silico* modelled interface modifications induced by mutations of VHH2 and 37D5 are shown in Fig. 1E-F.

2.3. Indirect ELISA and SPR of wildtype and mutant nanobodies

Nanobody binding affinity for their antigens was determined by ELISA and SPR. As illustrated in Fig. 2, ELISA test indicated that all

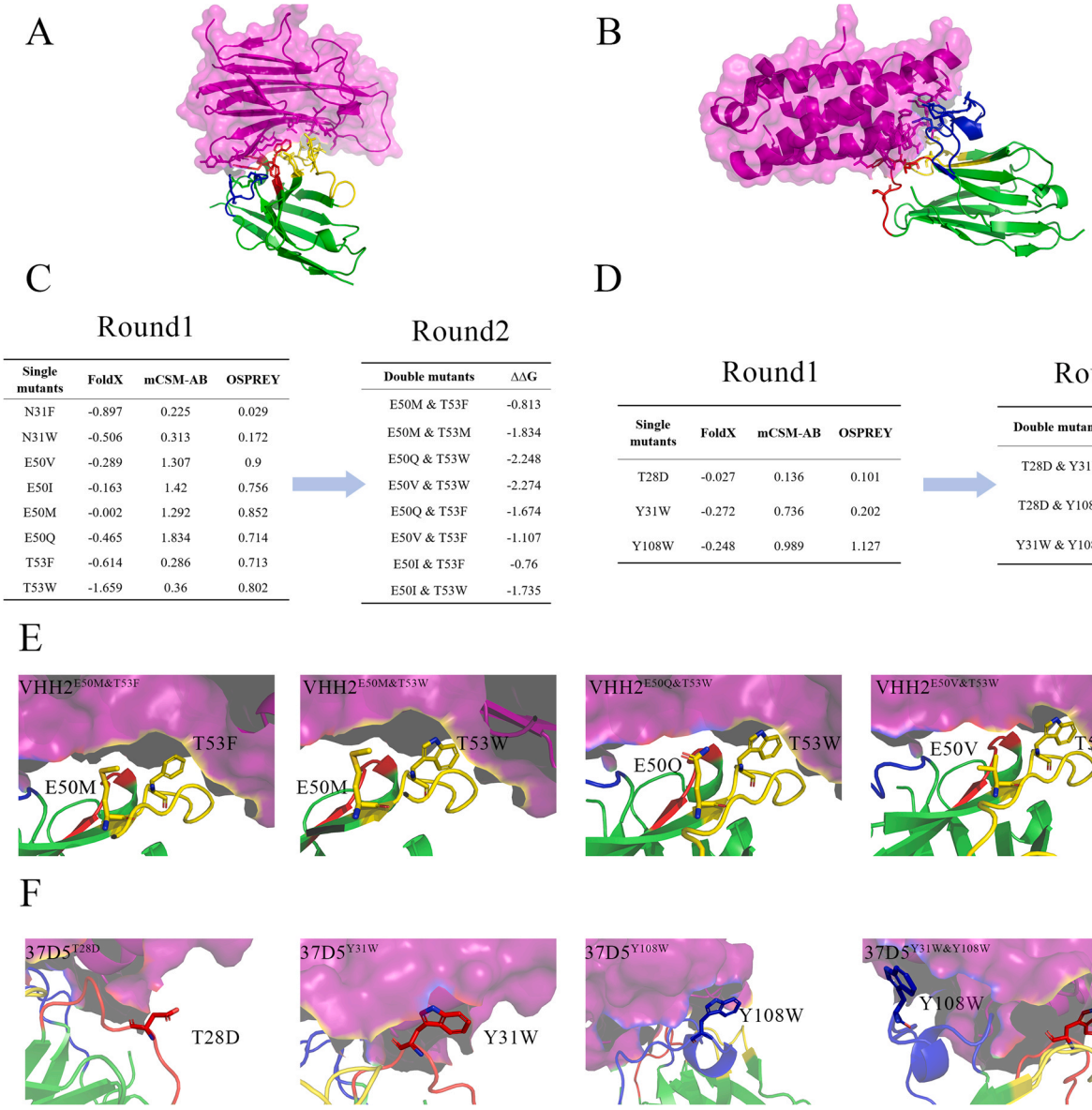

Single mutants	FoldX	mCSM-AB	OSPREY
N31F	-0.897	0.225	0.029
N31W	-0.506	0.313	0.172
E50V	-0.289	1.307	0.9
E50I	-0.163	1.42	0.756
E50M	-0.002	1.292	0.852
E50Q	-0.465	1.834	0.714
T53F	-0.614	0.286	0.713
T53W	-1.659	0.36	0.802

Double mutants	ΔΔG
E50M & T53F	-0.813
E50M & T53M	-1.834
E50Q & T53W	-2.248
E50V & T53W	-2.274
E50Q & T53F	-1.674
E50V & T53F	-1.107
E50I & T53F	-0.76
E50I & T53W	-1.735

Single mutants	FoldX	mCSM-AB	OSPREY
T28D	-0.027	0.136	0.101
Y31W	-0.272	0.736	0.202
Y108W	-0.248	0.989	1.127

Double mutants	ΔΔG
T28D & Y31W	0.451
T28D & Y108W	0.072
Y31W & Y108W	-0.118

Fig. 1. Antigen-nanobody docking interface and VIMAS-based mutation flow chart. (A) Structure of the VHH2-TNF-α complex. TNF-α is shown in purple, VHH2 in green. CDR1, CDR2, and CDR3 regions are shown in red, yellow and blue, respectively. (B) Structure of the 37D5-IL-23 complex, IL-23 is in purple, 37D5 in green. CDR1, CDR2, and CDR3 regions are shown in red, yellow and blue, respectively. (C) Two-round computational mutagenesis for VHH2 (eight double-residue mutants). (D) Two-round computational mutagenesis for 37D5 (three double-residue mutants). (E) Interface modifications of VHH2 mutants as predicted *in silico*. (F) Interface modifications of 37D5 mutants as predicted *in silico*. (For interpretation of the references to color in this figure legend, the reader is referred to the web version of this article.)

Table 2
Intrinsic solubility score of VHH2, 37D5 and their single-residue mutants as predicted by Camsol.

Nanobody	Intrinsic solubility score
VHH2	0.382
VHH2-N31F	-0.078
VHH2-N31W	-0.068
VHH2-E50V	0.128
VHH2-E50I	0.16
VHH2-E50M	0.23
VHH2-E50Q	0.312
VHH2-T53F	0.236
VHH2-T53W	0.24
37D5	0.535
37D5-T28D	0.754
37D5-Y31W	0.487
37D5-Y108W	0.528

VHH2 mutants had higher binding capacity than the wild type. Specifically, the experimentally determined concentrations corresponding to 50 % of the binding activity of the two best candidates $VHH2^{E50M\&T53F}$ and $VHH2^{E50M\&T53W}$ were 0.051 and 0.083 μg/ml. In the case of 37D5, the highest affinity was obtained by the double residue mutant $37D5^{Y31W\&Y108W}$ that scored a value of 0.15 μg/ml, whereas the binding of the three single-residue mutants did not differ significantly from that of the wildtype.

K_D values were then calculated by SPR using a Biacore T200 (Table 3 and Supplementary Fig. S2). Under the used experimental conditions, the K_D of VHH2 wild type corresponded to 11.2 nM (Fig. 3A), whereas that of the best mutant $VHH2^{E50Q\&T53W}$ was 2.9 nM, namely 3.9 times higher. All the other tested mutants resulted slightly better binders than the wild type, with K_D values of 4.6, 3.8, and 4.6 nM, respectively (Fig. 3A).

The K_D of 37D5 wild type was 3.9 nM (Fig. 3B) and the binding affinity of the best mutant $37D5^{Y31W\&Y108W}$ was only negligibly

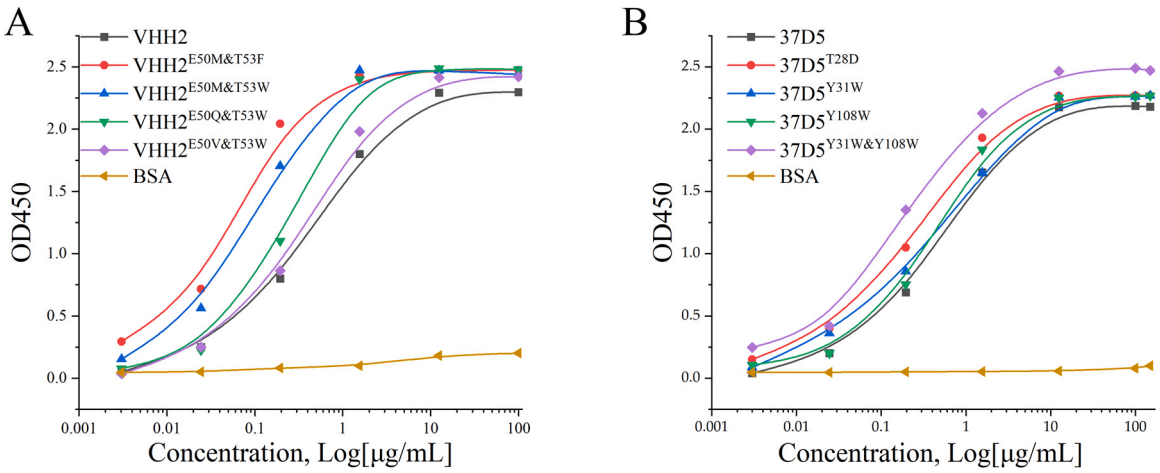

Fig. 2. ELISA assessment of nanobody/antigen binding. (A) Binding curves of TNF-α with VHH2 wildtype and mutants; (B) Binding curves of IL-23 with 37D5 wildtype and mutants. The VHH2/VHH2 mutant concentrations were 100, 12.5, 1.5625, 0.1953, 0.0244, 0.003 μg/ml. An additional concentration (200 μg/ml) was used for the experiments with 37D5 and its mutants.

Table 3
Kinetic constants of wild type and mutant nanobodies.

Nanobodies	ka (1/Ms)	kd (1/s)	K_D (nM)	Chi^2 (RU^2)
VHH2-TNF-α	4.2×10^5	4.7×10^{-3}	11.2	0.6
$VHH2^{E50M\&T53F}$-TNF-α	4.1×10^6	1.9×10^{-2}	4.6	1.0
$VHH2^{E50M\&T53W}$-TNF-α	2.9×10^6	1.1×10^{-2}	3.8	0.3
$VHH2^{E50Q\&T53W}$-TNF-α	2.6×10^6	7.3×10^{-3}	2.9	0.3
$VHH2^{E50V\&T53W}$-TNF-α	4.4×10^6	1.7×10^{-2}	3.9	1.0
37D5-IL-23	3.8×10^6	1.5×10^{-2}	3.9	0.1
$37D5^{T28D}$-IL-23	9.1×10^5	2.9×10^{-3}	3.2	0.2
$37D5^{Y31W}$-IL-23	1.3×10^6	4.2×10^{-3}	3.2	0.3
$37D5^{Y108W}$- IL-23	1.4×10^6	3.6×10^{-2}	2.6	0.4
$37D5^{Y31W\&Y108W}$- IL-23	3.4×10^6	5.9×10^{-3}	1.7	0.4

improved (1.7 nM, corresponding to a 2.7 K_D increase). The K_D of the remaining three single residue mutants was substantially unaffected (3.2, 3.2 and 2.6 nM, respectively, Fig. 3B). The trend was evidenced by both ELISA and SPR data appeared in good agreement. But, since the differences between wild type and mutants were reduced in terms of absolute values, the SPR measurements were repeated slightly modifying the experimental conditions (range of reagent concentrations, temperature, see Supplementary Fig. S3 and Table S11) and the resulting data further confirmed the improved binding of the mutants.

2.4. Thermal stability measurement for wide type and mutant nanobodies

Differential scanning fluorimetry (DSF) was used to determine the thermal stability of nanobodies and their mutants (Fig. 3C-D). The Tm of VHH2 wild type was 59.4 °C, whereas mutants showed higher stability (66.2, 66.1, 65.9 and 66.8 °C, respectively). The Tm value of 37D5 wild type was 64.5 °C and its mutants had similar characteristics (65, 64.5, 64.6 and 63.5 °C, respectively). Altogether, these data confirmed that mutations introduced for increasing the nanobody affinity did not affect negatively their stability and could even increase it.

2.5. Structural features of mutants

The analysis of the three-dimensional structures of the $VHH2^{E50Q\&T53W}$-TNF-α and $37D5^{Y31W\&Y108W}$-IL-23 complexes allows explaining the variations of affinity with respect to the wild type constructs (Figs. 4 and 5).

When VHH2-E50 was mutated to Q50, one side chain-side chain hydrogen bond was created with TNF-α-E135 (Fig. 4A). The spatial reorganization of the mutant $VHH2^{E50Q\&T53W}$ enabled the residue W32 to form a hydrophobic interaction with TNF-α-I97 (distance of 4.2 Å, Fig. 4B). A new main chain-side chain hydrogen bond emerged between $VHH2^{E50Q\&T53W}$-W53 and TNF-α-N137 (distance of 2.77 Å, Fig. 4C), as well as a cation-pi interaction between $VHH2^{E50Q\&T53W}$-W53 and TNF-α-R138 (distance of 5.0 Å, Fig. 4D).

In the $37D5^{Y31W\&Y108W}$-IL-23 complex, the hydrogen bond distance between nanobody-E101 and antigen-L97 diminished from 3.1 to 2.8 Å. In addition, the hydrogen bond distance between nanobody-S54 and antigen-D99 was reduced from 3.13 to 2.5 Å (Fig. 5A). Also the distance of the salt bridge between 37D5-E112 and IL-23-H29 decreased from 6.0 to 5.0 Å after mutation. A new salt bridge (5.7 Å) was formed between $37D5^{Y31W\&Y108W}$-D114 and IL-23-H29 (Fig. 5B) and Fig. 5C depicts a new aromatic-aromatic interaction between nanobody-F27 and antigen-Y115 (6.3 Å). The cation-pi interaction between the 37D5-Y31 and IL-23-K20 was preserved between $37D5^{Y31W\&Y108W}$-W31 and IL-23-K20 but the distance was shortened from 5.8 Å to 5.5 Å. At the same time, $37D5^{Y31W\&Y108W}$-R104 and IL-23-F90 formed a new cation-Pi interaction with a distance of 4.6 Å (Fig. 5D). Thus, a combination of shortened salt bridge distances and the formation of new aromatic and cation-pi interactions was the key for the enhanced affinity of $37D5^{Y31W\&Y108W}$ for its antigen.

2.6. Homology modeling, MD simulation and Molecular Docking of bispecific constructs

Once characterized the single and double mutants independently, nanobodies specific for the two antigens were combined into bispecific constructs. Several format designs were conceived that considered the reciprocal position at the N/C term as well as the type and length of the linker (Table 4). Their structures were modelled using Colabfold and Alphafold2 and evaluated using Verify 3D values, ERRAT plot, and Ramachandran plot in web server SAVES v6.0 (Supplementary Table S12). MD simulation was then applied to minimize their energy and Gromacs was used to analyze the root-mean-square deviation (RMSD). As shown in Supplementary Fig. S4, structures seem to have reached an equilibrium after 20 ns and it was possible obtaining high-quality homology models with stable conformation. Bispecific ligands were analyzed by HADDOCK and classified into clusters of models with variable Z-scores. Among these, the ones with lowest Z-score were

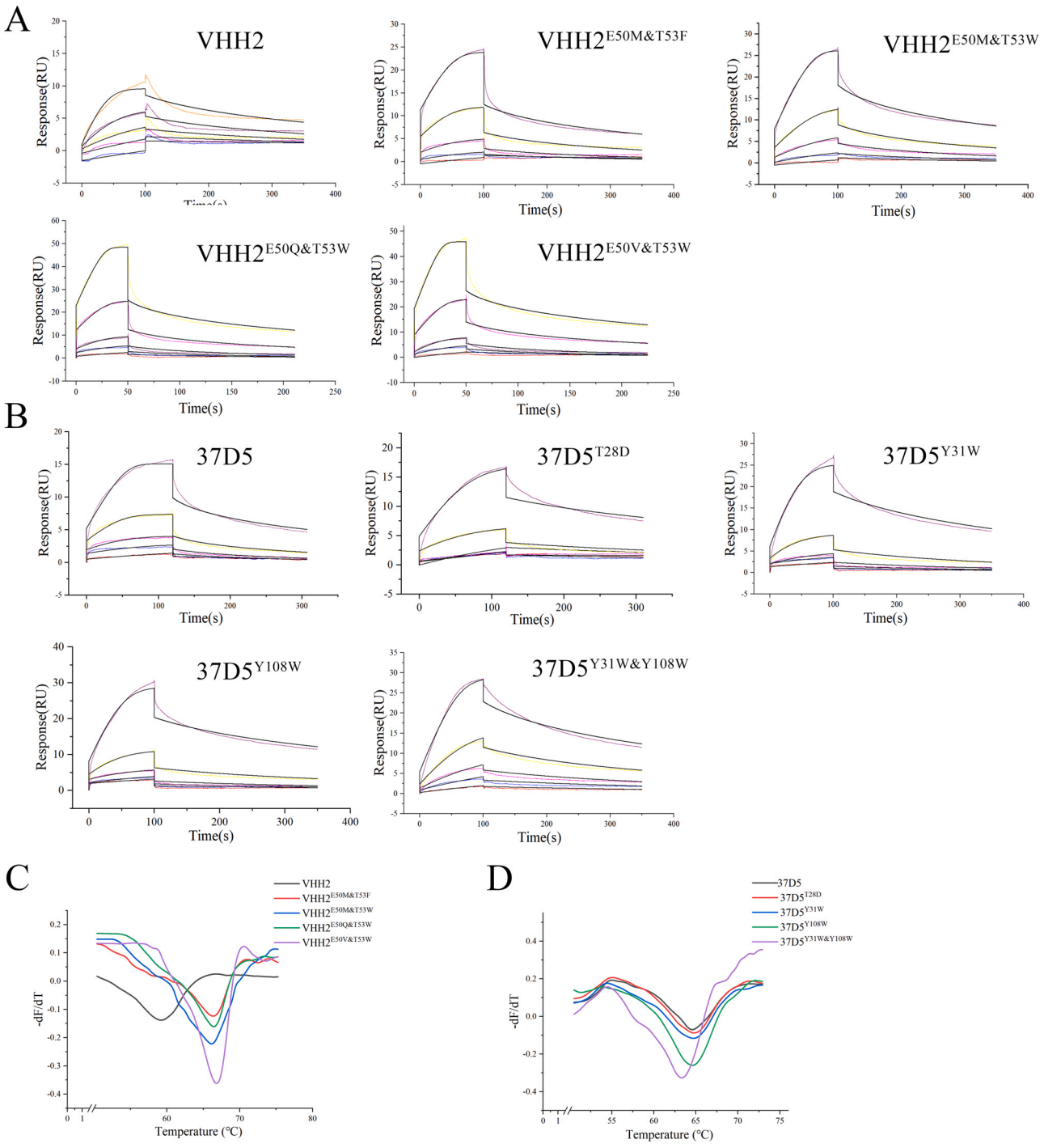

Fig. 3. Affinity and thermal stability analyses of wild type and mutant nanobodies. (A) SPR sensograms of VHH2 and its mutants; (B) SPR sensorgrams of 37D5 and its mutants; (C) Melting curves of VHH2 and its mutants; (D) Melting curves of 37D5 and its mutants.

selected for umbrella sampling simulation experiments to determine PMF and ΔG_{Bind} values (Table 5).

Antigens were classified as group B and bispecific binders as group A during the pulling step, then all atoms of group B were restricted to the origin and group A was pulled away from the complex with a spring force of 2000 kJ mol^{-1} nm^{-2}. The COM distance between the two groups gradually increased as the simulation time increased (Fig. 6 A). In this step, 501 configurations were generated, 21 were selected based on the 0.2 nm increase in COM spacing, and 10 ns molecular simulation was performed.

The difference between the PMF curve equilibrium value and the PMF minimum value can be used to estimate the antigen-nanobody binding energy (ΔG_{Bind}). As shown in Fig. 6B and Table 5, the ΔG_{Bind} of Bsn1 and Bsn3–1 to IL-23 were − 13.5, and − 15 kcal/mol, respectively. It could be seen that when 37D5Y31W&Y108W was placed at the N-terminus (Bsn3–1), the binding energy to IL-23 was slightly higher. The ΔG_{Bind} of Bsn1, Bsn3–1 and TNF-α were − 14 and − 35 kcal/mol, respectively (Fig. 6 C), and when $VHH2^{E50M\&T53F}$ was placed at the C-terminus of the construct (Bsn3–1) its binding to TNF-α was apparently increased, suggesting that $VHH2^{E50M\&T53F}$ should be placed at the C-terminus of the bispecific construct.

Once established that the most suitable sequence arrangement was $37D5^{Y31W\&Y108W}$ -linker- $VHH2^{E50M\&T53F}$, several linkers with different features in terms of length and composition were

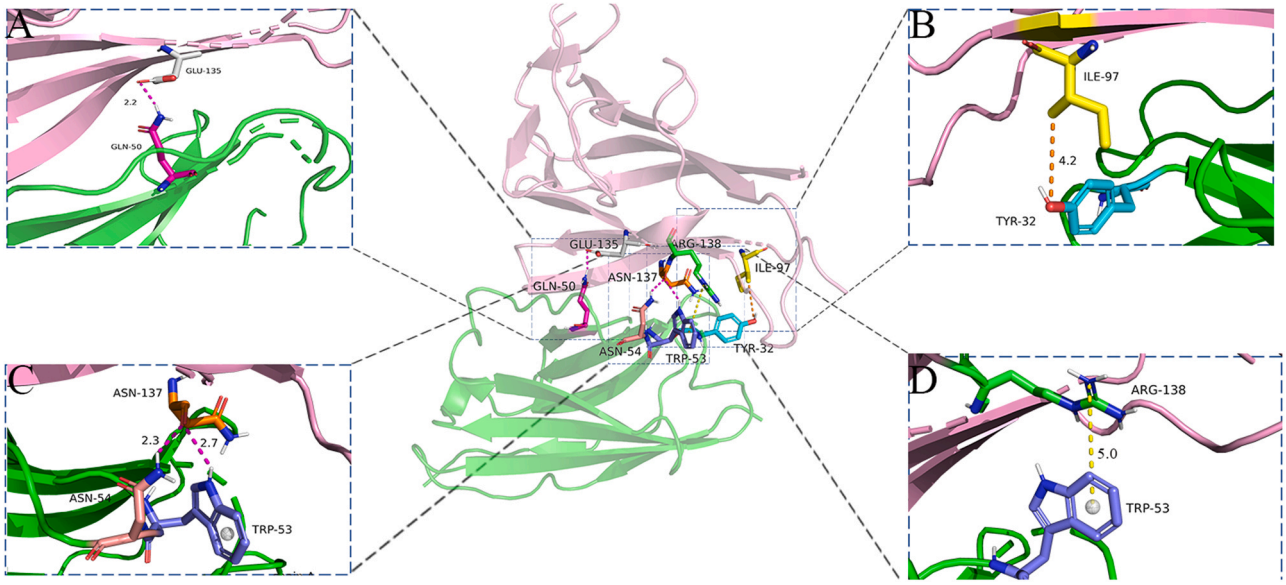

Fig. 4. Structure models of VHH2$^{E50Q\&T53W}$-TNF-α interactions. VHH2$^{E50Q\&T53W}$ and TNF-α are colored green and pink, respectively. (A) Side chain -Side chain hydrogen bond. (B) Hydrophobic interaction. (C) Main chain -Side chain hydrogen bonds. (D) Cation-Pi interaction. (For interpretation of the references to color in this figure legend, the reader is referred to the web version of this article.)

compared (Table 4). Specifically, rigid (EAAAK) and flexible (GGGGS) sequences repeated 2, 3 and 5 times were tested.

When constructs with flexible linkers were compared, the data reported in Fig. 6D-E show that the binding energy of Bsn3–1 to TNF-α was substantially lower than that of Bsn2 and Bsn4 (ΔG_{Bind} of −35, −13, and −12.5 Kcal/mol, respectively). When rigid linkers were used, the ΔG_{Bind} of Bsn5, Bsn6 and Bsn7 was − 17.5, − 21 and − 15 Kcal/mol, respectively. Altogether, the data suggested that the best combination is a flexible linker of intermediate length.

The *in silico* predictions were verified by ELISA experiments aimed at determining the affinity of Bsn1 and Bsn3–1 for IL-23, and affinity of Bsn1, 2, 3–1, 4 to TNF-α, respectively. The results (Supplementary Fig. S5) showed that Bsn3–1 had the highest combined affinity. Other constructs were excluded by this characterization step because no or scarcely soluble.

The antigen-bispecific construct interactions were analyzed by FoldX (Table 6) and the analysis of the interface between Bsn3–1 and

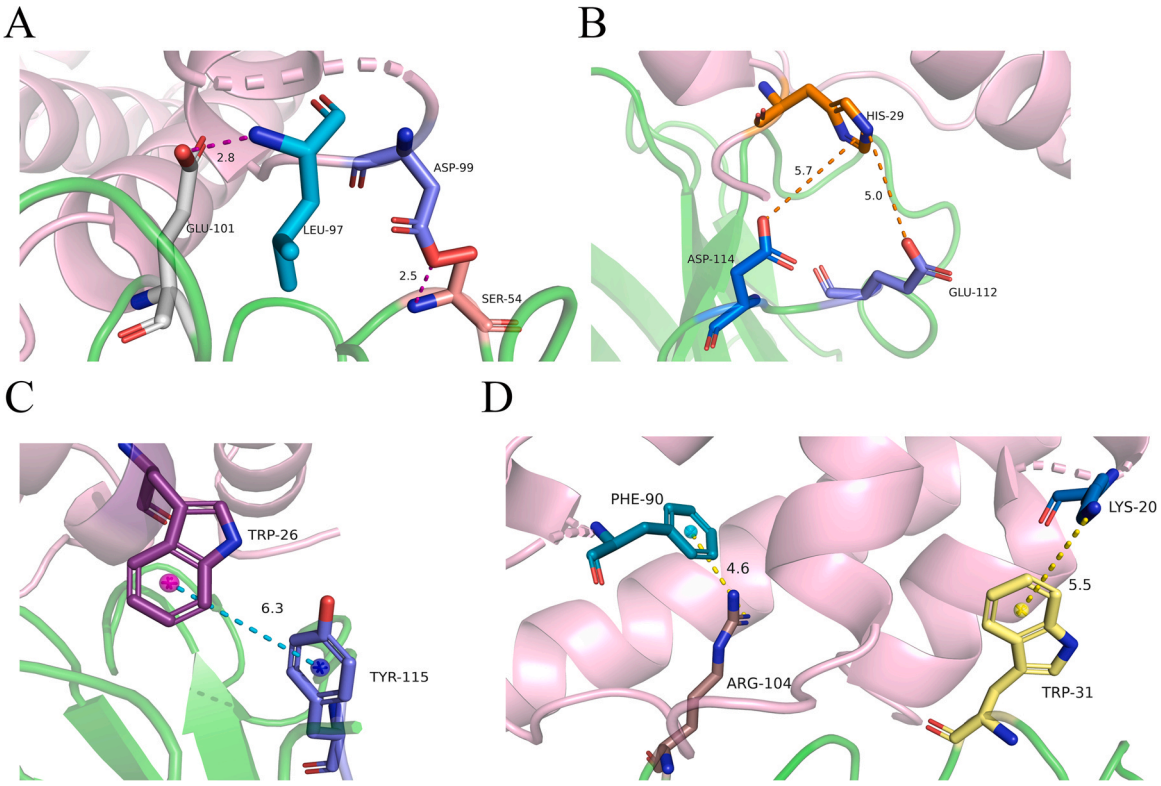

Fig. 5. Structure models of 37D5$^{Y31W\&Y108W}$-IL-23 interactions. 37D5$^{Y31W\&Y108W}$ and IL-23 are colored green and pink, respectively. (A) Hydrogen bond. (B) Salt bridges. (C) Aromatic-Aromatic interaction. (D) Cation-Pi interaction. (For interpretation of the references to color in this figure legend, the reader is referred to the web version of this article.)

Table 4
Bispecific constructs used for *in silico* valuation.

Number	Bispecific constructs sequences
Bsn1	VHH2$^{E50M\&T53F}$-$(GGGGS)_3$-37D5$^{Y31W\&Y108W}$
Bsn2	37D5$^{Y31W\&Y108W}$-GGGSGGGGS-VHH2$^{E50M\&T53F}$
Bsn3–1	37D5$^{Y31W\&Y108W}$-$(GGGGS)_3$-VHH2$^{E50M\&T53F}$
Bsn4	37D5$^{Y31W\&Y108W}$-$(GGGGS)_5$-VHH2$^{E50M\&T53F}$
Bsn5	37D5$^{Y31W\&Y108W}$-$(EAAAK)_2$-VHH2$^{E50M\&T53F}$
Bsn6	37D5$^{Y31W\&Y108W}$-A$(AEAAK)_3$A-VHH2$^{E50M\&T53F}$
Bsn7	37D5$^{Y31W\&Y108W}$-$(EAAAK)_5$-VHH2$^{E50M\&T53F}$

Table 5
Free binding energy of complexes between antigens and bispecific binders.

	ΔG_{Bind} (Kcal/mol)
Bsn1-IL-23	-13.5
Bsn3–1-IL-23	-15
Bsn1-TNF-α	-14
Bsn2-TNF-α	-13
Bsn3–1-TNF-α	-35
Bsn4-TNF-α	-12.5
Bsn5-TNF-α	-17.5
Bsn6-TNF-α	-21
Bsn7-TNF-α	-15

Table 6
Free energy of bispecific nanobodies by FoldX.

Docking complex	Energy (Kcal/mol)						
	ΔG	ΔE_{bh}	ΔE_{sh}	ΔE_{vdw}	ΔE_{ele}	ΔGpb	ΔG_{nb}
Bsn1-IL-23	-9.25	-4.13	-5.63	-21.46	-2.67	29.8	-27.8
Bsn3–1-IL23	-10.54	-1.83	-1.89	-13.29	0.64	15.62	-18.65
Bsn1-TNF-α	-7.37	-1.18	-5.29	-17.4	-1.11	22.94	-23.85
Bsn2-TNF-α	-12.28	-1.17	-6.34	-16.58	-0.62	20.47	-22.89
Bsn3–1-TNF-α	-15.74	-5.14	-11.62	-18.48	-0.61	23.8	-24.67
Bsn4-TNF-α	-14.12	-2.65	-5.06	-15.87	-0.03	16.88	-22.1
Bsn5-TNF-α	-10.47	-2.37	-3.24	-15.3	-0.95	18.55	-20.77
Bsn6-TNF-α	-11.19	-3.7	-8.23	-16.56	-0.1	21.7	-21.12
Bsn7-TNF-α	-10.49	-5.71	-8.79	-16.21	-1.7	22.91	-20.59

TNF-α (Fig. 7) showed the presence of five hydrogen bonds plus several van der Waals contacts.

2.7. Model bispecific binder characterization

The evaluation of the affinity of the anti-TNF-α nanobody mutants gave contrasting results when measured by ELISA or SPR. In the doubt, we decided to compair the bispecific construct Bsn3–1 (37D5$^{Y31W\&Y108W}$-$(GGGGS)_3$-VHH2$^{E50M\&T53F}$) with a new one called Bsn3–3, based on the alternative anti-TNF-α (37D5$^{Y31W\&Y108W}$-

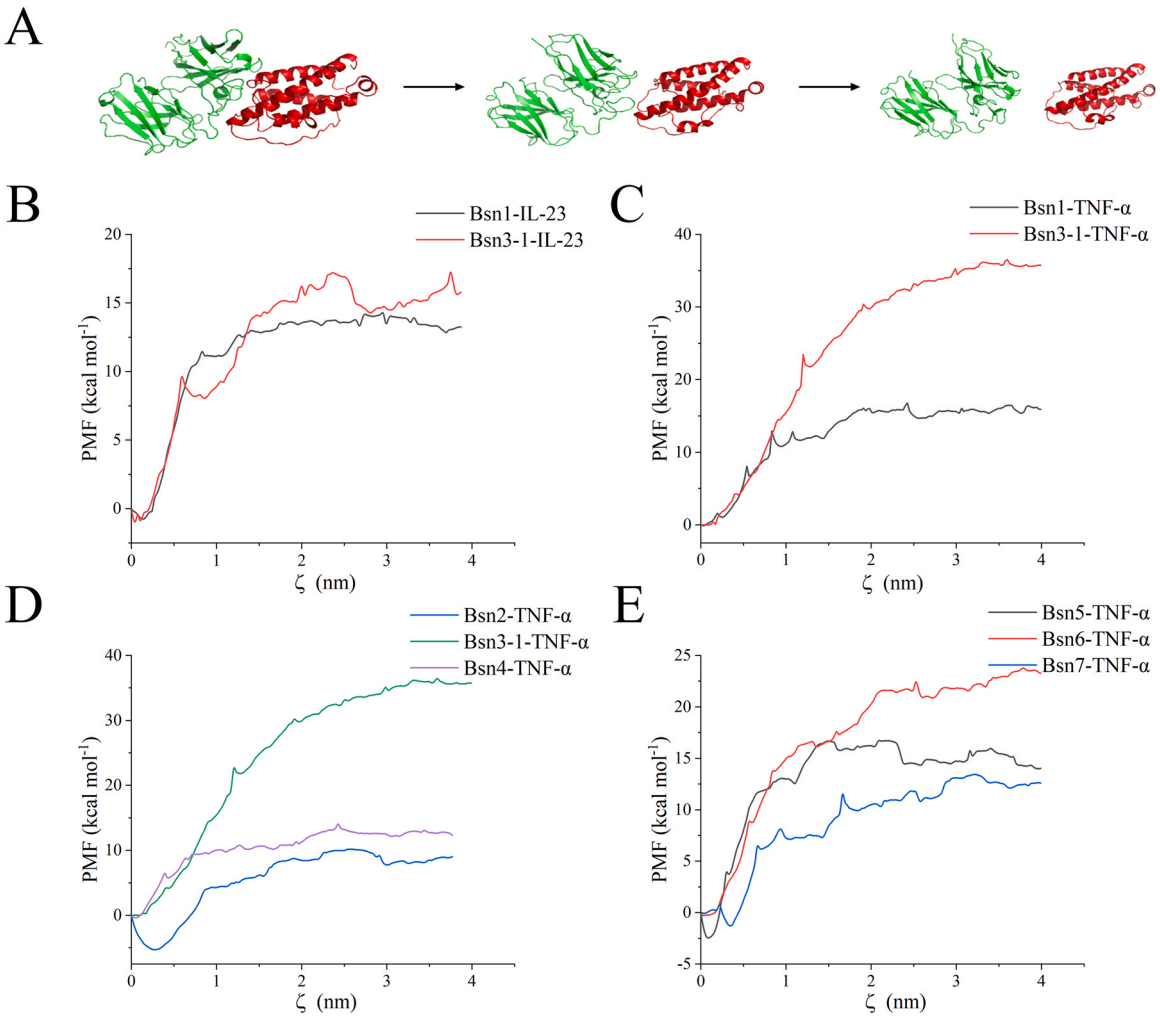

Fig. 6. Pulling step of pull and umbrella sampling simulation and PMF curve for the interaction of bispecific binders with antigens. (A) Pulling step of pull and umbrella sampling simulation. 1st, 250th, and 350th conformers excerpted from Pull and umbrella sampling simulation of Bsn1 with IL-23. (B) PMF curve for the interaction of Bsn1 and Bsn3–1 with IL-23. (C) PMF curve for the interaction of Bsn1 and Bsn3–1 with TNF-α. (D) PMF curve for the interaction of Bsn5, Bsn6 and Bsn7 with TNF-α. (E) PMF curve for the interaction of Bsn2, Bsn3–1 and Bsn4 with TNF-α.

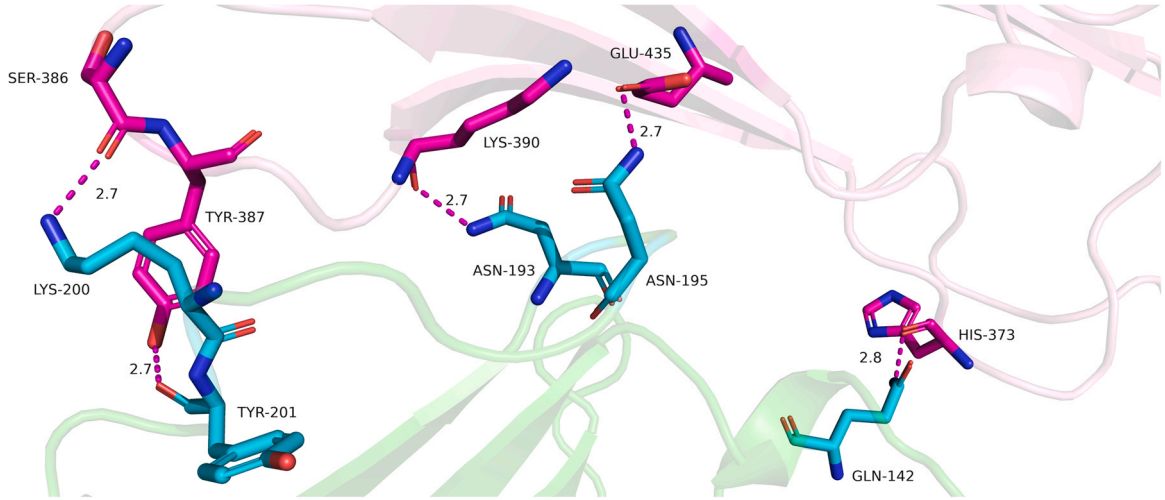

Fig. 7. Details of the interface between Bsn3–1 and TNF-α. Residues in Bsn3–1 are shown in cyan, those in TNF-α are magenta, and hydrogen bonds are purple. (For interpretation of the references to color in this figure legend, the reader is referred to the web version of this article.)

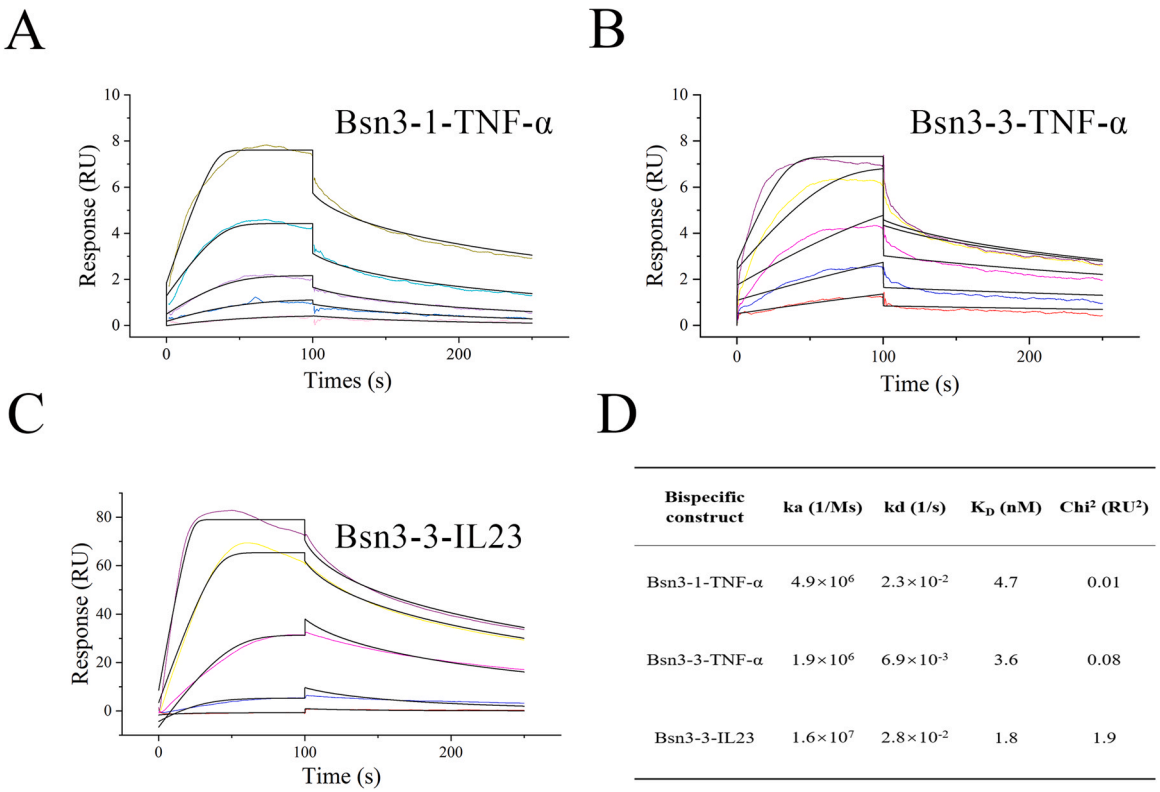

Bispecific construct	ka (1/Ms)	kd (1/s)	K_D (nM)	Chi² (RU²)
Bsn3-1-TNF-α	4.9×10^{6}	2.3×10^{-2}	4.7	0.01
Bsn3-3-TNF-α	1.9×10^{6}	6.9×10^{-3}	3.6	0.08
Bsn3-3-IL23	1.6×10^{7}	2.8×10^{-2}	1.8	1.9

Fig. 8. Bispecific constructs binding characterization. (A)-(B) SPR sensorgrams of bispecific constructs binding to TNF-α. (C) SPR sensorgram of bispecific constructs binding to IL23. (D) bispecific constructs kinetic values corresponding to the experiments reported in A and B.

$(GGGGS)_3$-VHH2$^{E50Q\&T53W}$). Such fusion proteins have a mass of approximately 31 kDa (Supplementary Fig. S6), and yielded of 0.38 and 0.25 mg/l, respectively. The two constructs had similar *KD* values but the dissociation rate of Bsn3–1 was more rapid than that of Bsn3–3 (Fig. 8 A, B, D). Therefore, Bsn3–3 was used for the successive biophysical and functional characterization. The two-domain construct did not affect negatively the biding affinity for IL-23 (Fig. 8).

The effective bispecific capacity of the construct was tested by ELISA. Plates were coated with either TNF-α or IL-23 alone, or with a 1:1 antigen mix. The estimated affinity values of Bsn3–3 were 10.3 nM for TNF-α, 12.9 nM for IL-23 but 1.1 nM for the antigen mix, indicating a clear avidity effect (Fig. 9).

Next the inhibitory effect of the bispecific construct on the TNF-α-dependent cytotoxicity was evaluated using the L929 cell line since it expresses the p55 receptor bound by TNF-α[35]. L929 cells were co-incubated with TNF-α and either Bsn3–3 or VHH2 for 24 h to test the biological activity of the nanobody. The results showed that VHH2 biological activity was preserved in the Bsn3–3 construct with an IC50 of 12 nM (Fig. 10A-B).

3. Discussion

The data reported in this work show a straightforward protocol to design a bifunctional construct targeting two macromolecules

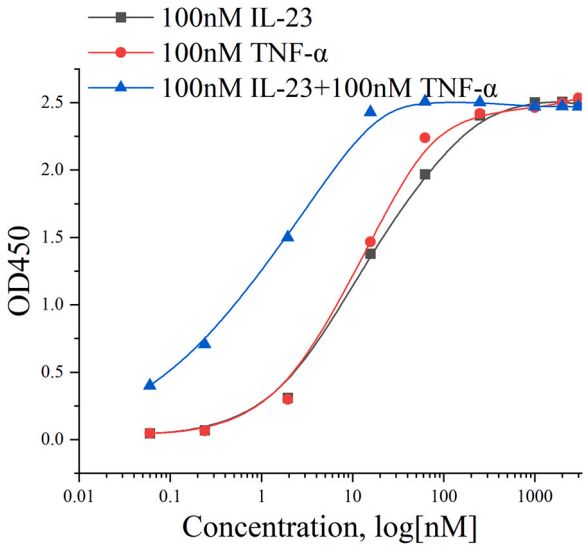

Fig. 9. Concentration-dependent ELISA assessment of binder/antigen interaction. The avidity effect promoted by the antigen co-presence confirms the binder functional bispecific characteristics.

(TNF-α and IL-23) that have been already independently considered for IBD, but represents a model that could be applied to any other biological question which requires the contemporary targeting of two different epitopes/molecules.

We applied the VIMAS approach to successfully increase the affinity of both involved nanobodies despite they already had *K*D in the low nanomolar range. This result was obtained with minimal mutagenesis (one or two residues) and is highly interesting for the perspectives it opens. So far, *in silico* affinity maturation of peptides and antibody fragments has been considered effective because enabled to increase significantly the binding capacity of the starting molecules[36–39]. However, the evaluation parameter was always relative, namely focused on the affinity gain, and not absolute, i.e. did not question the actual value of reached *K*D. However, whether the use of an algorithm allows passing from 100 μM to 500 nM of affinity can be considered meaningful from a scientific point of view, its practical advantage is questionable because the final binder would still have insufficient affinity for most of the biologically and clinically relevant applications. Looking at the available literature, it seems that *in silico* approaches applied to nanobodies hit a sort of invisible wall that blocked most of the attempts to increase the affinity when this reached the tens of nanomolar [40,41]. This has also to do with the often diverging development of affinity and stability, a reason for which becomes often impossible to produce soluble and correctly folded mutants with theoretical higher binding affinity [42]. The approach presented in this study overcomes this limit of one log and, surprisingly, does not affect negatively the nanobody thermal stability, although the yields of the nanobody variants produced recombinantly were generally lower than those of the wild types.

Another relevant contribution of this work is the approach for assessing the factors affecting the biological activity of bispecific nanobodies, such as their spatial organization determined by their reciprocal position and by the size and complexity of the linkers [43]. The accessibility of each nanobody to its specific antigen is a strong determinant and can be differently affected by the copresence of the second nanobody linked either to its N- or C- term. By modeling the different combinations, it was possible to identify the most favorable solutions. Specifically, the solvent-accessible surface area of Bsn1-TNF-α and Bsn3–1-TNF-α was determined being 1747.6 Å^2 and 2166.18 Å^2, respectively, a result that demonstrated the higher binding capacity of the second design. In combination with predictions that favored flexible linkers, it was then possible to design optimized bispecific constructs. Such constructs were also more stable than those which used rigid linkers. This point was not further investigated but the literature reports the reciprocal stabilizing effects that fusion proteins may exert when a flexible linker allows their surfaces to interact [44].

Methodologically, there is an important issue to consider, namely how to evaluate the mutant affinity, since this value can be significantly affected by the technique and instrumentation used to acquire the data, as already proved by other researchers [45,46]. To avoid method-based bias, we validated experimentally the *in silico* designed mutants by means of two orthogonal analytical techniques, ELISA and SPR. We noticed that some nanobodies performed clearly better in one specific experimental set with respect to the other. In the ELISA experiment, the antigen was coated on the 96-well plate by hydrophobic interactions with the polystyrene surface[47], whereas the chemistry used to coat the SPR involved lysine groups. Although the analysis of the consequences determined by this difference on the binding capacity of the single nanobodies would require an independent study, we tried at least a simulation that indeed indicated how the residues belonging to the interaction surface could be selectively affected by the presence of a

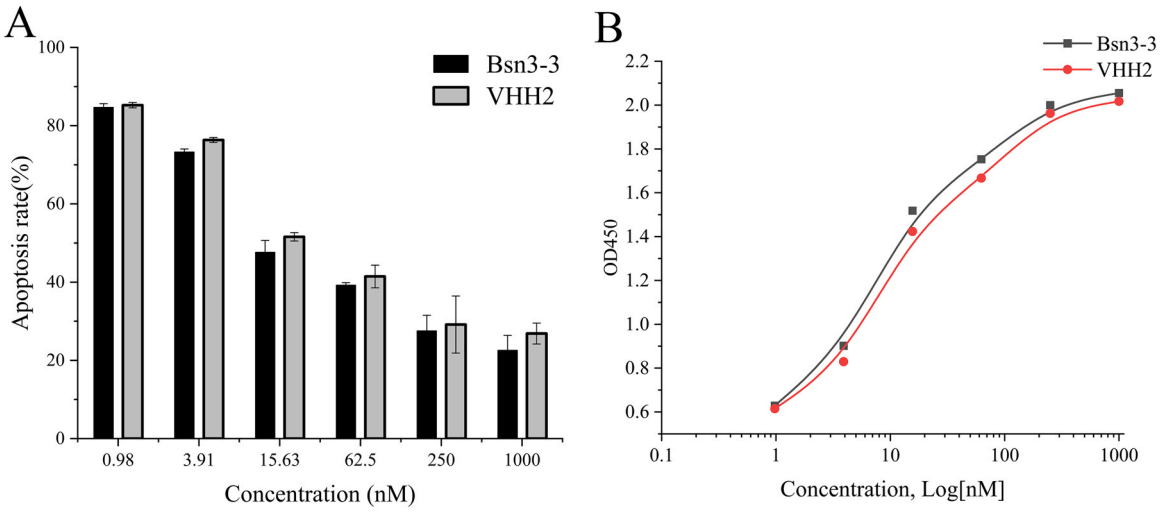

Fig. 10. Inhibition of TNF-α cytotoxicity by means of Bsn3–3 and VHH2. (A) Dose-dependent apoptosis inhibition in the presence of 5 μg/ml TNF-α. All data are represented as means ± SD; (B) Bsn3–3 and VHH2-dependent inhibition of TNF-cytotoxicity was evaluated using the CCK8 kit.

hydrophobic surface (Supplementary Fig. S7) [48]. Since it is difficult to predict what method for affinity measurement will be the most reliable for any specific molecule and mutant, we opted for testing experimentally more mutant options (Bsn3–1 & Bsn3–3, as reported in Fig. 8) when affinity indications were not unambiguous for their choice.

4. Materials and methods

4.1. Identification of the nanobody/antigen interface residues

The data corresponding to the three-dimensional structures of the anti-gen-nanobody complexes VHH2-TNF-α and 37D5-IL23 were downloaded from the PDB database (PDB ID 5M2J and 4GRW, respectively) [30,31]. Interface residues were automatically identified by InterProSurf [49](http://curie.utmb.edu/usercomplex.html) after having uploaded the data into the webserver.

4.2. In silico affinity maturation

The identification of mutations that should confer higher affinity to the original nanobodies was performed exploiting a method that combines the results obtained from three different available platforms which use alternative algorithms to determine their scores[50]. Specifically, such two-step approach (VIMAS[28]) first hypermutates any of the nanobody residues involved in the antigen binding (13 for VHH2 and 10 for 37D5) with all amino acids, with the exception of cysteine and proline. Later, applies the resulting single mutations (221 for VHH2 and 170 for 37D5) to the predictions of mCSM-AB, OSPREY and FoldX (software versions were supplied in the Supplementary Table S13) [32–34]. Data uploaded through the mCSM-AB web-server (http://biosig.unimelb.edu.au/mcsm_ab/prediction) allow evaluating the changes of Gibbs free energy for any single point mutation. OSPREY, a protein design soft-ware with Python interface, uses antigen-nanobody complexes optimized through MOL probity online server[51] to systematically mutate all the residues involved in the antigen-nanobody interactions and calculate the variation of binding free energy. FoldX runs as a plug-in in YASARA software, which provides a visualization window. First, the Repair object command enable to perform a step of energy minimization of the complex structure by testing amino acid mutations. Initially, the default parameters of the mutation program were used and the average of three results was used to reduce the errors and identify the values of Total energy and Interaction energy which represent the change in structural stability and binding free energy after mutation, respectively. Positive value variations in mCSM-AB and OSPREY, and negative in FoldX indicated lower binding free energy and potentially higher binding capacity. We finally selected the single-point mutations with highest scores obtained in all the three protocols (consensus mutations) for the next optimization step.

In parallel, to preserve the nanobody solubility during the process of affinity maturation, the effect of the mutations was evaluated by applying a CamSol analysis [52] and mutations that reduced the solubility were removed.

In a second optimization round, single residue mutations were combined systematically and the variation of free energy of double residue mutants was estimated by FoldX by using the Mutate multiple residues command. The mutants with decreased affinity were discarded and further experiments were performed with eight double mutations of VHH2 and one of 37D5, plus three single-residue mutants for 37D5.

4.3. Protein expression and purification

Nanobody sequences were cloned into pET-32a (+) vector to obtain constructs with a C-terminal 6xHis tag. Expression plasmids were transformed in *Trans*B (DE3) E. coli. Antigens were cloned in PcDNA3.1 (+) and expressed in HEK293 cells. The purification of all nanobodies was by Ni^{2+}-affinity chromatography combining a 5 ml HisTrap™ HP column (Cytiva) and an AKTA Prime Plus, whereas the purification of antigens exploited the glutathione affinity for the GST tag, using a 5 ml GST-Trap™ column (Cytiva). Nanobody fractions from affinity purification underwent size exclusion chromatography (SEC) on a 24 ml SuperdexTM 75 increase 10/300 GL (Cytiva). The nanobody homogeneity was evaluated by 12 % SDS-PAGE electrophoresis.

4.4. Binding activity of mutants quantified byt ELISA

One hundred μl of purified antigens TNF-α and IL-23 were added to 96-well plates at a concentration of 10 μg/ml and incubated overnight at 4 °C. After three washing steps in PBST (PBS plus 0.05 % w/v Tween-20), 200 μl of blocking solution (5 % skim milk powder in PBS) were added to each well, the plates were incubated 2 h at 37 °C, the blocking solution was discarded, then 100 μl of nanobodies at different concentrations (200, 150, 100, 12.5, 1.5625, 0.1953, 0.0244, 0.003 μg/ml, in PBS) were added before incubating for 2 h at 37 °C. After washing, anti-His-tag secondary anti-bodies fused to horseradish peroxidase (1:10,000 in PBS) were added and incubated for 1 h at 37 °C. The enzymatic activity was detected in the presence of TMB Two-Component Substrate solution kit (Solarbio®, Beijing, China). Specifically, 100 μl of TMB solution were added to each well and incubated 20 min at 37 °C, the reaction was terminated by adding 100 μl of 1 M H2SO4. Absorbance signals were measured at 450 nm and data processed with Origin 2021.

4.5. Binding affinity of mutants quantified by SPR

Experiments were performed using a Biacore T200. TNF-α and IL-23 were diluted to 5 μg/ml with pH 4.0 and pH 4.5 sodium acetate solution, respectively, and immobilized on CM5 chips following the directions of the Immobilization Wizard program. The target levels of TNF-α and IL-23 were set at 1000 RU and 1500 RU, respectively. Nanobodies (at concentrations of 200, 100, 50, 25, 12.5, 6.25, 3.125, 1.5625 nM) were injected over the chip either at a flow rate of 30 μl/min for 100 s, or at a flow rate of 60 μl/min for 50 s. Contact time was 120 s and dissociation time was 400–600 s, glycine-HCl (pH 1.5 or 2.5) was used to regenerate the chip at a flow rate of 30 μg/ml for 90 s. Data were analyzed with the manufacturer's software, using five concentration values for each sample, the KD value was calculated with 1:1 binding model. Experiments were repeated increasing the ligand concentrations to reach 2000 RU, and evaluating the effect of temperature, increased from 25° to 37°C.

4.6. Thermal stability measurement for nanobodies

Differential scanning fluorimetry (DSF) was used to determine the Tm value of nanobodies and their mutants. The overall sample volume was of 20 μl, nanobodies were diluted in PBS to 2 μM and added to a 96-well plate in the presence of 1.0 μl HEPES (1 M), 0.04 μl TCEP (0.25 M), 6.67 μl NaCl (0.9 M) and 0.5 μl SYPRO® Orange, then made up with ddH2O to 20 μl. Reactions were carried out in a Roche Light-Cycler® 480 II real-time PCR instrument setting the excitation wavelength was 465 nm, the emission at 580 nm, the temperature gradient ranged from 25° to 95°C, with Continuous Acquisition Mode, the Ramp Rate of 0.01 °C/s, and the Acquisitions per °C at 100.

4.7. Homology modeling, molecular dynamics simulation and molecular docking

Bispecific constructs were designed adopting linkers with variable characteristics in terms of length and composition, such as $(GGGGS)_2$, $(GGGGS)_3$, $GGGGS)_5$, $(AEAAK)_2$, $(AEAAK)_3$ and (AEAAK), and were modeled using Colabfold and Alphafold2 [53] (https://colab.research.google.com/github/sokrypton/ColabFold/blob/main/AlphaFold2.ipynb) that provided five models for each sequence. These were submitted t to web server SAVE v6.0 (https://saves.mbi.ucla.edu/) to select the best one in each group for the molecular dynamics simulation.

All bispecific construct MD simulations were performed in GROMACS 2019.5 applying AMBER99SB-ILDN force field, placing the model in a cuboid of simple point charge (SPC) water with the shortest distance from the model to the edge of the box of 1.2 nm and in the presence of Na^+ and Cl^- (0.15 M) to balance the ionization. After following the steepest descents minimization, the system was equilibrated by canonical ensemble (NVT) for 100 ps. In this process, temperature was maintained at 300 K using the velocity-rescale thermostat, and then the system was equilibrated by isothermal-isobaric ensemble (NPT) for 100 ps, using Parrinello-Rahman barostat to maintain pressure isotropically at 1.0 bar [54]. Finally, the iteration time step with LINCS (Linear Constraint Solver) constraint was set to 2 fs. Using periodic boundary conditions, the MD simulations of all mutant models were run for 50 ns (except for Bsn7 which was run for 100 ns). The bispecific construct models obtained from the MD simulation were used as the initial model for molecular docking.

The webserver HADDOCK was used to dock antigen and bispecific constructs [55]. We uploaded the structure files of antigens and binders to the webserver (https://alcazar.science.uu.nl/services/HADDOCK2.2/haddock.php), specifying active residues of both antigens and bispecific constructs and nine docking complexes were described.

4.8. Umbrella sampling simulation and analysis of binding free energy of bispecific constructs by FoldX

The docking structures built by HADDOCK were used as references for pulling simulation. Once placed the structure in a suitable GROMACS box, the antigen was regarded as a fixed B group and used as an immobile reference for pulling simulations, whereas bispecific constructs were regarded as an A group. After 100 ps of MD simulation in NPT ensemble at 300 K and 1 bar, A group was pulled along the x-axis with a spring constant of 2000 kJ $mol^{-1}nm^{-2}$ and a pull rate of 0.1 nm ps^{-1} for 500 ps. After the end of pulling, the trajectories based on the final center-of-mass (COM) distance between groups A and B (approximately 4 nm) were selected for sampling windows at 0.2 nm intervals. Snapshots were taken to generate the starting configuration of the umbrella sampling window [56]. Twenty-one configurations were taken out from the pulling trajectory in different reaction coordinates for each of these configurations. After each window was equilibrated by NPT ensemble for 100 ps at 300 K and 1 bar, 10 ns of MD was performed (total simulation time: 210 ns) and was utilized for umbrella sampling. The weighted histogram analysis method (WHAM) was used for result analysis and to obtain the potential of mean force (PMF) of antigen-nanobody complex necessary to calculate the free energy of binding [57]. Umbrella sampling simulations were performed for all nine complexes.

The repair object command of FoldX was used to perform energy minimization on the nine groups of docking complexes by rearranging the side chains of amino acid residues. The FoldX interaction energy of molecules function enabled to calculate the binding free energy (ΔG), backbone hydrogen bond energy (ΔE_{bh}), sidechain hydrogen bond energy (ΔE_{sh}), Van der Waals force (ΔE_{vdw}), electrostatic interaction (ΔE_{ele}), polar solvent-free energy (ΔG_{pb}) and Nonpolar solvent-free energy (ΔG_{nb}) of nanobodies.

4.9. Protein expression and purification of bispecific constructs

Umbrella sampling simulation and analysis of binding free energy allowed the identification of the fittest format for the bispecific construct (37D5-$(GGGGS)_3$-VHH2) that was expressed and purified as previously described for single nanobodies (Section 4.3).

4.10. Affinity measurement of bispecific constructs

The affinity of bispecific constructs was quantified by SPR, applying the conditions described above, and by ELISA using, 96-well plates coated with 100 μl of TNF-α, IL-23 or a mix of both at a molar concentration of 100 nM. The analyte concentrations were 3000, 2000, 1000, 250, 62.5, 15.63, 1.95, 0.24, 0.06 nM, otherwise the protocol was as in 4.4.

4.11. Cytotoxicity assay

L929 cells were cultured in DMEM medium containing 10 % fetal bovine serum, 1 % penicillin and 1 % streptomycin. One hundred μl of cells (50,000 cells/ml) were added to microplate wells (plate A) and incubated for 24 h at 37 °C in humidified atmosphere and 5 % CO_2. In a second 96-well plate (Plate B), either 50 μl of 5 μg/ml TNF-α or 50 μl of VHH2 and Bsn3–3 at different dilutions were added to each well and incubated for 2 h at 37 °C. Plate A was washed with DMEM medium and 100 μl of the mixed solutions from plate B were added, whereas 100 μl of DMEM medium containing 1 % bovine serum was used as a control. The plate was kept in the incubator for 24 h, washed twice with the medium before the addition of 10 μl of CCK8 solution. The plate was incubated at 37 °C for 4 h, the absorbance signals were measured at 450 nm and data processed with Origin 2021.

5. Conclusions

The present study describes a strategy to optimize the biophysical features on nanobodies by means of the VIMAS platform and to design nanobody constructs able to target simultaneously two independent antigens. The obtained affinity increases may be considered limited in absolute terms, but were applied to binders that already possessed *K*D in the low nanomolar range. Furthermore, the increased affinities were paired with a significant gain in terms of thermostability. When nanobodies for two independent antigens were combined in a single construct, this proved possessing bispecific functionality, provided an avidity effect quantifiable in the gain of a log of EC50 concentration towards targets displaying both antigens and prevented TNF-mediated apoptosis in L929 cells in vitro. Our is a rational concept for the development of reagents for dual-target therapy suitable for approaching a large array of diseases [18].

Funding

The present study was supported by grants from the National Key Research and Development Project (Grant No. 2019YFA0905600), the Science and Technology Program of Tianjin, China (Grant No. 19YFSLQY00110), the Major State Basic Research Development Program of the Natural Science Foundation of Shandong Province in China (Grant No. ZR2020ZD11), and by the grant ARRS/P3-0428 provided by the Javna Agencija za Raziskovalno Dejavnost Republike Slovenije. We thank Shaoxing “MingShiZhiXiang” Meritocrat Project for its support.

Institutional review board statement

Not applicable.

Informed consent statement

Not applicable.

CRediT authorship contribution statement

Conceptualization, **Zixuan Bai, Jiewen Wang** and **He Huang**; Data curation, **Zixuan Bai, Jiewen Wang, Jiaqi Li, Haibin Yuan, Xiangtong Cao, Xiangan Cao** and **Ario Marco**; Formal analysis, **Zixuan Bai, Guangbo Kang** and **He Huang**; Funding acquisition, **He Huang**; Investigation, **Zixuan Bai, Jiewen Wang** and **Miao Zhang**; Methodology, **Zixuan Bai, Jiewen Wang, Guangbo Kang** and **Ario Marco**; Project administration, **He Huang**; Resources, **Ping Wang, Yuanhang Feng** and **He Huang**; Software, **Zixuan Bai, Jiewen Wang** and **Jiaqi Li**; Supervision, **He Huang**; Validation, **Zixuan Bai, Jiewen Wang, Guangbo Kang** and **He Huang**; Visualization, **Jiewen Wang** and **Ario Marco**; Writing – original draft, **Zixuan Bai** and **Ario Marco**; Writing – review & editing, **Zixuan Bai, Jiewen Wang, Jiaqi Li, Haibin Yuan, Miao Zhang, Guangbo Kang, Ario Marco** and **He Huang**. All authors have read and agreed to the published version of the manuscript.

Data availability statement

Not applicable.

Conflict of interest

Authors P.W. was employed by Tianjin Modern Innovative TCM Technology Co. Ltd. Authors M.Z. was employed by China Resources Biopharmaceutical Company Limited. The remaining authors declare that the research was conducted in the absence of any commercial or financial relationships that could be construed as a potential conflict of interest.

Appendix A. Supporting information

Supplementary data associated with this article can be found in the online version at doi:10.1016/j.csbj.2022.12.021.

References

[1] Baumgart DC, Sandborn WJ. Crohn's disease. Lancet 2012;380:1590–605. https://doi.org/10.1016/S0140-6736(12)60026-9

[2] Ordas I, Eckmann L, Talamini M, Baumgart DC, Sandborn WJ. Ulcerative colitis. Lancet 2012;380:1606–19. https://doi.org/10.1016/S0140-6736(12)60150-0

[3] Feagan BG, Sandborn WJ, D'Haens G, Panes J, Kaser A, Ferrante M, et al. Induction therapy with the selective interleukin-23 inhibitor risankizumab in patients with moderate-to-severe Crohn's disease: a randomised, double-blind, placebo-controlled phase 2 study. Lancet 2017;389:1699–709. https://doi.org/10.1016/S0140-6736(17)30570-6

[4] Lim WC, Wang Y, MacDonald JK, Hanauer S. Aminosalicylates for induction of remission or response in Crohn's disease. Cochrane Database Syst Rev 2016;7:1–60. https://doi.org/10.1002/14651858.CD008870

[5] Colombel JF, Sandborn WJ, Reinisch W, Mantzaris GJ, Kornbluth A, Rachmilewitz D, et al. Infliximab, azathioprine, or combination therapy for Crohn's disease. N Engl J Med 2010;362:1383–95. https://doi.org/10.1056/NEJMoa0904492

[6] Hanauer SB, Feagan BG, Lichtenstein GR, Mayer LF, Schreiber S, Colombel JF, et al. Maintenance infliximab for Crohn's disease: the ACCENT I randomised trial. Lancet 2002;359:1541–9. https://doi.org/10.1016/S0140-6736(02)08512-4

[7] Colombel JF, Rutgeerts PJ, Sandborn WJ, Yang M, Camez A, Pollack PF, et al. Adalimumab induces deep remission in patients with Crohn's disease. Clin Gastroenterol Hepatol 2014;12:414–22. https://doi.org/10.1016/j.cgh.2013.06.019

[8] Targan SR, Feagan BG, Fedorak RN, Lashner BA, Panaccione R, Present DH, et al. Natalizumab for the treatment of active Crohn's disease: results of the ENCORE Trial. Gastroenterology 2007;132:1672–83. https://doi.org/10.1053/j.gastro.2007.03.024

[9] Feagan BG, Sandborn WJ, Gasink C, Jacobstein D, Lang Y, Friedman JR, et al. Ustekinumab as induction and maintenance therapy for Crohn's disease. N Engl J Med 2016;375:1946–60. https://doi.org/10.1056/NEJMoa1602773

[10] Sands BE, Sandborn WJ, Van Assche G, Lukas M, Xu J, James A, et al. Vedolizumab as induction and maintenance therapy for Crohn's disease in patients naive to or who have failed tumor necrosis factor antagonist therapy. Inflamm Bowel Dis 2017;23:97–106. https://doi.org/10.1097/Mib.0000000000000979

[11] Ben-Horin S, Chowers Y. Tailoring anti-TNF therapy in IBD: drug levels and disease activity. Nat Rev Gastroenterol Hepatol 2014;11:243–55. https://doi.org/10.1038/nrgastro.2013.253

[12] Guerra I, Bermejo F. Management of inflammatory bowel disease in poor responders to infliximab. Clin Exp Gastroenterol 2014;7:359–67. https://doi.org/10.2147/CEG.S45297

[13] Schmitt H, Billmeier U, Dieterich W, Rath T, Sonnewald S, Reid S, et al. Expansion of IL-23 receptor bearing TNFR2+ T cells is associated with molecular resistance to anti-TNF therapy in Crohn's disease. Gut 2019;68:814–28. https://doi.org/10.1136/gutjnl-2017-315671

[14] Ng SC, Shi HY, Hamidi N, Underwood FE, Tang W, Benchimol EI, et al. Worldwide incidence and prevalence of inflammatory bowel disease in the 21st century: a systematic review of population-based studies. Lancet 2017;390:2769–78. https://doi.org/10.1016/S0140-6736(17)32448-0

[15] Sands BE, Chen JJ, Feagan BG, Penney M, Rees WA, Danese S, et al. Efficacy and safety of MEDI2070, an antibody against interleukin 23, in patients with moderate to severe Crohn's disease: a phase 2a study. Gastroenterology 2017;153:77–86. https://doi.org/10.1053/j.gastro.2017.03.049

[16] Rawla P, Sunkara T, Raj JP. Role of biologics and biosimilars in inflammatory bowel disease: current trends and future perspectives. J Inflamm Res 2018;11:215–26. https://doi.org/10.2147/JIR.S165330

[17] Lim SI. Fine-tuning bispecific therapeutics. Pharmacol Ther 2020;212:1–13. https://doi.org/10.1016/j.pharmthera.2020.107582

[18] Wang J, Kang G, Yuan H, Cao X, Huang H, de Marco A. Research progress and applications of multivalent, multispecific and modified nanobodies for disease treatment. Front Immunol 2021;12:838082https://doi.org/10.3389/fimmu.2021.838082

[19] Hamers-Casterman C, Atarhouch T, Muyldermans S, Robinson G, Hamers C, Songa EB, et al. Naturally occurring antibodies devoid of light chains. Nature 1993;363:446–8. https://doi.org/10.1038/363446a0

[20] De Vos J, Devoogdt N, Lahoutte T, Muyldermans S. Camelid single-domain antibody-fragment engineering for (pre)clinical in vivo molecular imaging applications: adjusting the bullet to its target. Expert Opin Biol Ther 2013;13:1149–60. https://doi.org/10.1517/14712598.2013.800478

[21] Svecova D, Lubell MW, Casset-Semanaz F, Mackenzie H, Grenningloh R, Krueger JG. A randomized, double-blind, placebo-controlled phase 1 study of multiple ascending doses of subcutaneous M1095, an anti-interleukin 17A/F nanobody, in moderate-to-severe psoriasis. J Am Acad Dermatol 2019;81:196–203. https://doi.org/10.1016/j.jaad.2019.03.056

[22] Arbabi-Ghahroudi M, Tanha J, MacKenzie R. Prokaryotic expression of antibodies. Cancer Metastasis Rev 2005;24:501–19. https://doi.org/10.1007/s10555-005-6193-1

[23] Sliwkowski MX, Mellman I. Antibody therapeutics in cancer. Science 2013;341:1192–8. https://doi.org/10.1126/science.1241145

[24] Soler MA, Medagli B, Semrau MS, Storici P, Bajc G, de Marco A, et al. A consensus protocol for the in silico optimisation of antibody fragments. Chem Commun 2019;55:14043–6. https://doi.org/10.1039/c9cc06182g

[25] Lippow SM, Wittrup KD, Tidor B. Computational design of antibody-affinity improvement beyond in vivo maturation. Nat Biotechnol 2007;25:1171–6. https://doi.org/10.1038/nbt1336

[26] Vivcharuk V, Baardsnes J, Deprez C, Sulea T, Jaramillo M, Corbeil CR, et al. Assisted design of antibody and protein therapeutics (ADAPT. PLoS One 2017;12:1–17. https://doi.org/10.1371/journal.pone.0181490

[27] Cheng X, Wang J, Kang G, Hu M, Yuan B, Zhang Y, et al. Homology modeling-based in silico affinity maturation improves the affinity of a nanobody. Int J Mol Sci 2019;20:1–19. https://doi.org/10.3390/ijms20174187

[28] Hu M, Kang G, Cheng X, Wang J, Li R, Bai Z, et al. In vitro affinity maturation to improve the efficacy of a hypoxia-inducible factor 1alpha single-domain intrabody. Biochem Biophys Res Commun 2020;529:936–42. https://doi.org/10.1016/j.bbrc.2020.06.097

[29] Kang G, Hu M, Ren H, Wang J, Cheng X, Li R, et al. VHH212 nanobody targeting the hypoxia-inducible factor 1alpha suppresses angiogenesis and potentiates gemcitabine therapy in pancreatic cancer in vivo. Cancer Biol Med 2021;18:772–87. https://doi.org/10.20892/j.issn.2095-3941.2020.0568

[30] Desmyter A, Spinelli S, Boutton C, Saunders M, Blachetot C, de Haard H, et al. Neutralization of human interleukin 23 by multivalent nanobodies explained by the structure of cytokine-nanobody complex. Front Immunol 2017;8:884. https://doi.org/10.3389/fimmu.2017.00884

[31] Beirnaert E, Desmyter A, Spinelli S, Lauwereys M, Aarden L, Dreier T, et al. Bivalent Llama single-domain antibody fragments against tumor necrosis factor have picomolar potencies due to intramolecular interactions. Front Immunol 2017;8:867. https://doi.org/10.3389/fimmu.2017.00867

[32] Schymkowitz J, Borg J, Stricher F, Nys R, Rousseau F, Serrano L. The FoldX web server: an online force field. Nucleic Acids Res 2005;33:W382–8. https://doi.org/10.1093/nar/gki387

[33] Pires DE, Ascher DB. mCSM-AB: a web server for predicting antibody-antigen affinity changes upon mutation with graph-based signatures. Nucleic Acids Res 2016;44:W469–73. https://doi.org/10.1093/nar/gkw458

[34] Hallen MA, Martin JW, Ojewole A, Jou JD, Lowegard AU, Frenkel MS, et al. OSPREY 3.0: open-source protein redesign for you, with powerful new features. J Comput Chem 2018;39:2494–507. https://doi.org/10.1002/jcc.25522
[35] Nie J, Ma X, Hu F, Miao H, Feng X, Zhang P, et al. Designing and constructing a phage display synthesized single domain antibodies library based on camel VHHs frame for screening and identifying humanized TNF-alpha-specific nanobody. Biomed Pharmacother 2021;137:1–11. https://doi.org/10.1016/j.biopha.2021.111328
[36] Wang Z, Li Y, Liang W, Zheng J, Li S, Hu C, et al. A highly sensitive detection system based on proximity-dependent hybridization with computer-aided affinity maturation of a scFv antibody. Sci Rep 2018;8:3837. https://doi.org/10.1038/s41598-018-22111-4
[37] Cannon DA, Shan L, Du Q, Shirinian L, Rickert KW, Rosenthal KL, et al. Experimentally guided computational antibody affinity maturation with de novo docking, modelling and rational design. PLoS Comput Biol 2019;15:e1006980https://doi.org/10.1371/journal.pcbi.1006980
[38] Akiba H, Tamura H, Caaveiro JMM, Tsumoto K. Computer-guided library generation applied to the optimization of single-domain antibodies. Protein Eng Des Sel 2019;32:423–31. https://doi.org/10.1093/protein/gzaa006
[39] Wang X, Chen Q, Sun Z, Wang Y, Su B, Zhang C, et al. Nanobody affinity improvement: Directed evolution of the anti-ochratoxin A single domain antibody. Int J Biol Macromol 2020;151:312–21. https://doi.org/10.1016/j.ijbiomac.2020.02.180
[40] Jeliazkov JR, Sljoka A, Kuroda D, Tsuchimura N, Katoh N, Tsumoto K, et al. Repertoire analysis of antibody CDR-H3 loops suggests affinity maturation does not typically result in rigidification. Front Immunol 2018;9:413. https://doi.org/10.3389/fimmu.2018.00413
[41] Julian MC, Li L, Garde S, Wilen R, Tessier PM. Efficient affinity maturation of antibody variable domains requires co-selection of compensatory mutations to maintain thermodynamic stability. Sci Rep 2017;7:45259. https://doi.org/10.1038/srep45259
[42] Sormanni P, Aprile FA, Vendruscolo M. Third generation antibody discovery methods:in silicorational design. Chem Soc Rev 2018;47:9137–57. https://doi.org/10.1039/c8cs00523k
[43] Zhang JH, Yun J, Shang ZG, Zhang XH, Pan BR. Design and optimization of a linker for fusion protein construction. Prog Nat Sci Mater 2009;19:1197–200. https://doi.org/10.1016/j.pnsc.2008.12.007
[44] Chen XY, Zaro JL, Shen WC. Fusion protein linkers: property, design and functionality. Adv Drug Deliv Rev 2013;65:1357–69. https://doi.org/10.1016/j.addr.2012.09.039
[45] Rich RL, Papalia GA, Flynn PJ, Furneisen J, Quinn J, Klein JS, et al. A global benchmark study using affinity-based biosensors. Anal Biochem 2009;386:194–216. https://doi.org/10.1016/j.ab.2008.11.021
[46] Fournout S, Jouin P, Pau B, Hanin V. Comparison of different immunoenzymatic methods for the determination of the fine specificity and affinity constants of polyclonal antibodies against pseudopeptide haptens. Immunol Investig 1997;26:549–59. https://doi.org/10.3109/08820139709088539
[47] Engvall E, Perlmann P. Enzyme-linked immunosorbent assay (ELISA). Quantitative assay of immunoglobulin G. Immunochemistry 1971;8:871–4. https://doi.org/10.1016/0019-2791(71)90454-x
[48] Hagemans D, van Belzen IA, Moran Luengo T, Rudiger SG. A script to highlight hydrophobicity and charge on protein surfaces. Front Mol Biosci 2015;2:56. https://doi.org/10.3389/fmolb.2015.00056
[49] Negi SS, Schein CH, Oezguen N, Power TD, Braun W. InterProSurf: a web server for predicting interacting sites on protein surfaces. Bioinformatics 2007;23:3397–9. https://doi.org/10.1093/bioinformatics/btm474
[50] Sulea T, Hussack G, Ryan S, Tanha J, Purisima EO. Application of assisted design of antibody and protein therapeutics (ADAPT) improves efficacy of a Clostridium difficile toxin A single-domain antibody. Sci Rep 2018;8:1–11. https://doi.org/10.1038/s41598-018-20599-4
[51] Williams CJ, Headd JJ, Moriarty NW, Prisant MG, Videau LL, Deis LN, et al. MolProbity: more and better reference data for improved all-atom structure validation. Protein Sci 2018;27:293–315. https://doi.org/10.1002/pro.3330
[52] Soler MA, Medagli B, Wang J, Oloketuyi S, Bajc G, Huang H, et al. Effect of humanizing mutations on the stability of the llama single-domain variable region. Biomolecules 2021;11:1–13. https://doi.org/10.3390/biom11020163
[53] Jumper J, Evans R, Pritzel A, Green T, Figurnov M, Ronneberger O, et al. Highly accurate protein structure prediction with AlphaFold. Nature 2021;596:583–9. https://doi.org/10.1038/s41586-021-03819-2
[54] Lee H. Effects of nanoparticle electrostatics and protein-protein interactions on corona formation: conformation and hydrodynamics. Small 2020;16:1–10. https://doi.org/10.1002/smll.201906598
[55] van Zundert GCP, Rodrigues J, Trellet M, Schmitz C, Kastritis PL, Karaca E, et al. The HADDOCK2.2 web server: user-friendly integrative modeling of biomolecular complexes. J Mol Biol 2016;428:720–5. https://doi.org/10.1016/j.jmb.2015.09.014
[56] Lemkul JA, Bevan DR. Assessing the stability of alzheimer's amyloid protofibrils using molecular dynamics. J Phys Chem B 2010;114:1652–60. https://doi.org/10.1021/jp9110794
[57] Shankar K, Djamal B, Robert HS, Peter AK. THE weighted histogram analysis method for free-energy calculations on biomolecules. I. The method. J Comput Chem 1992;13:1011–21. https://doi.org/10.1002/jcc.540130812